Supplemental Appendix for Coarse-Grained Fundamental Forms for Characterizing Isometries of Trapezoid-based Origami Metamaterials

James P. McInerney* and Xiaoming Mao
Department of Physics, University of Michigan, Ann Arbor, MI 48109, USA

Diego Misseroni
Department of Civil, Environmental, and Mechanical Engineering, University of Trento, Trento 38123, Italy

D. Zeb Rocklin
School of Physics, Georgia Institute of Technology, Atlanta, GA 30332, USA

Glaucio H. Paulino
Department of Civil and Environmental Engineering, Princeton University, Princeton, NJ, 08544 and Princeton Materials Institute (PMI), Princeton University, Princeton, NJ, 08544
(Dated: September 6, 2024)

LATTICE COMPATIBILITY

This appendix discusses the generators of a quasi-cylindrical origami tessellation. First, we discuss the ground state compatibility conditions and their implications that enforce quasi-cylindrical geometries for periodic tessellations. Second, we discuss the infinitesimal changes to the lattice generators induced by an isometry of the underlying crease pattern. These results largely follow from Refs. [1, 2].

Zeroth-order Compatibility

Consider an origami tessellation that is periodic in both the sector angles and the dihedral angles, such as that shown in Fig. 1(A), with cell indices denoted (n_1, n_2). We denote the primitive lattice vectors $(\boldsymbol{\ell}_1, \boldsymbol{\ell}_2)$ and the primitive lattice rotation matrices $(\mathbf{S}_1, \mathbf{S}_2)$, with corresponding rotation axes $(\hat{S}_1, \hat{S}_2)$ and *finite* lattice rotation angles (η_1, η_2). The lattice rotations are necessarily identical in each cell because they depend exclusively on the periodic sector angles and dihedral angles. However, the lattice vectors rotate between cells according to the lattice rotations. For the tessellation to have a unique position and orientation in each cell, the generators must satisfy the orientation and position compatibility conditions illustrated in Fig. 1B and Fig. 1C respectively:

$$\mathbf{S}_1\mathbf{S}_2 = \mathbf{S}_2\mathbf{S}_1, \tag{1}$$

$$\boldsymbol{\ell}_1 + \mathbf{S}_1\boldsymbol{\ell}_2 = \boldsymbol{\ell}_2 + \mathbf{S}_2\boldsymbol{\ell}_1, \tag{2}$$

The implication of orientation compatibility in Eqn. (1) is that the lattice rotations are coaxial $\hat{S}_1 = \hat{S}_2 \equiv \hat{S}$ so that the lattice vector along the μ lattice direction in the (n_1, n_2) cell is $\boldsymbol{\ell}_\mu(n_1, n_2) = \mathbf{S}_1^{n_1}\mathbf{S}_2^{n_2}\boldsymbol{\ell}_\mu = \mathbf{S}_2^{n_2}\mathbf{S}_1^{n_1}\boldsymbol{\ell}_\mu$, or any alternating product thereof. The implication of position compatibility in Eqn. (2) is that the sheet has a unique radius of curvature, which we show by first considering the radii of curvature measured along the two lattice directions denoted R_1 and R_2. We define the radius of curvature along a particular lattice direction as the radius of the osculating circle that connects a point in adjacent cells, which must be constant because of the periodicity in the angles of the tessellation. The radius is dependent on the point of the cell the osculating circle connects, which is equivalent to the statement that the lattice vectors are dependent on the choice of the vertex basis vectors. We calculate this radius of curvature via the geometry of chords (see Fig. 1D, where we illustrate two different radii):

$$R_\mu = \frac{|\boldsymbol{\ell}\mu^\perp|}{2\sin(\eta_\mu/2)}, \tag{3}$$

* james.mcinerney.5.ctr@afrl.af.mil

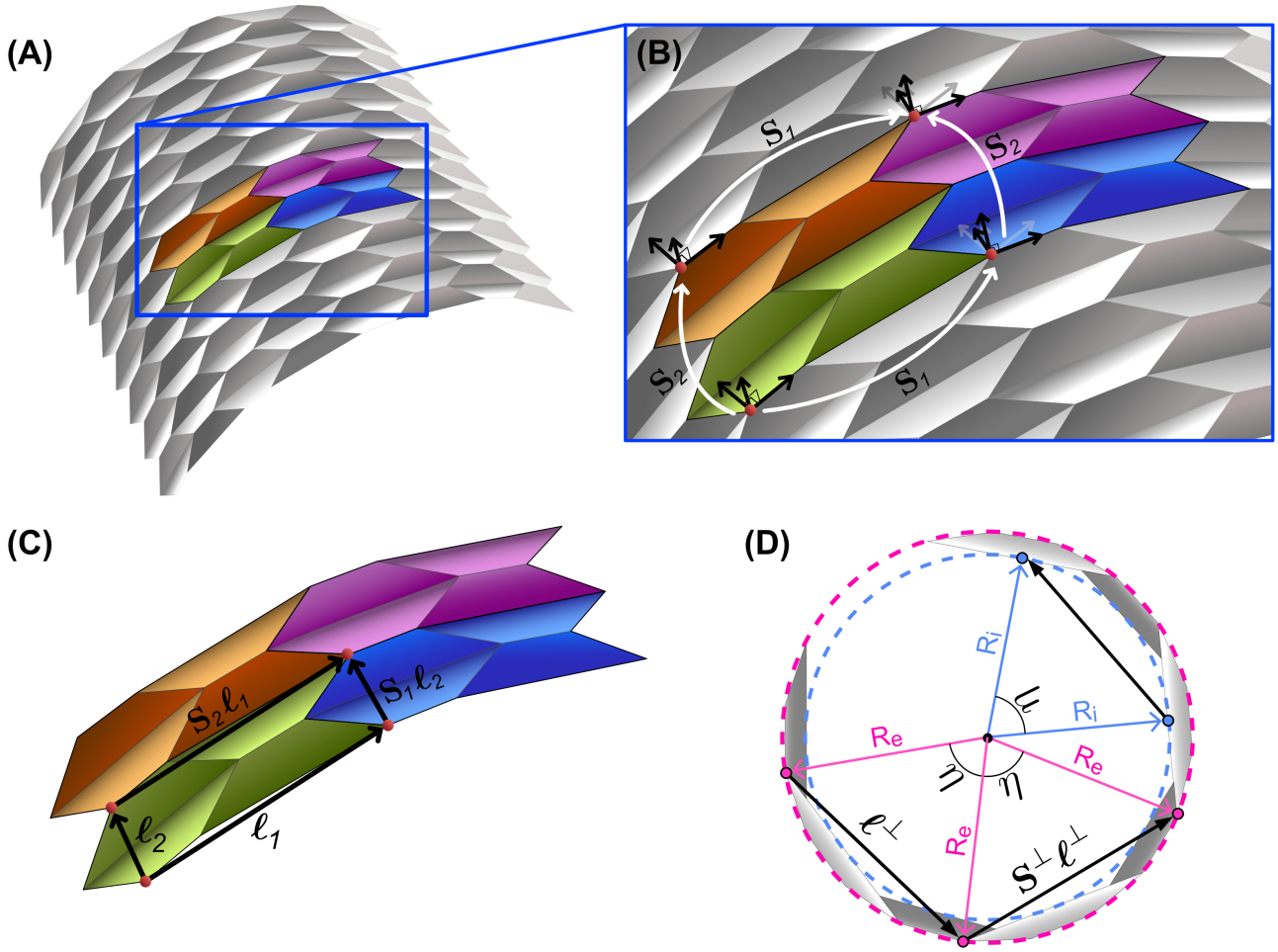

FIG. 1. Illustration of the lattice generators and the lattice compatibility conditions. (A) An example quasi-cylindrical ground state from a geometry that is periodic in the sector angles and the dihedral angles. Each of the four colors highlights an adjacent cell. (B) Illustration of the orientation compatibility condition imposed on the lattice rotation matrices $\mathbf{S}_{1,2}$. (C) Illustration of the position compatibility condition imposed on the lattice vectors $\boldsymbol{\ell}_{1,2}$ and the lattice rotations. (D) A top-down view of the tessellation in panel A labeling the lattice rotation angle η, the in-plane components of the lattice vectors $\boldsymbol{\ell}^\perp$ and lattice rotations $\mathbf{S}^\perp$, and the radii measured from the outermost point R_e and the innermost point R_i of the tessellation.

where we use the superscript $\perp$ to denote the components of the lattice vector in the plane normal to the lattice rotation axis: $\boldsymbol{\ell}_\mu^\perp \equiv \boldsymbol{\ell}_\mu - (\boldsymbol{\ell}_\mu \cdot \hat{S})\hat{S}$. For the lattice rotations, $\mathbf{S}_\mu^\perp$, this superscript indicates the rotation within the plane defined by $\hat{S}$. Since position compatibility in Eqn. (2) enforces

$$\boldsymbol{\ell}_2^\perp = (\mathbf{1} - \mathbf{S}_1^\perp)^{-1}(\mathbf{1} - \mathbf{S}_2^\perp)\boldsymbol{\ell}_1^\perp \tag{4}$$

Eqn. (3) yields the same result for either lattice direction $R_1 = R_2 \equiv R$. Thus, the ground states of the origami tessellations we consider form cylindrical sections, with symmetry axis $\hat{S}$ and radius R. The self-intersection, or locking, of these cylindrical sections depends on the number of cells in the tessellation and only special geometries allow for rigid folding after imposing closure of the cylinder. Lastly, the position of a vertex in cell (n_1, n_2) with basis vertex position $\mathbf{r}_i$ in the unit cell is then given by discrete integration over the path to the vertex:

$$\mathbf{r}_i(n_1, n_2) = \mathbf{S}_1^{n_1}\mathbf{S}_2^{n_2}\mathbf{r}_i + \sum_{n=0}^{n_1-1} \mathbf{S}_1^n\boldsymbol{\ell}_1 + \mathbf{S}_1^{n_1}\sum_{n=0}^{n_2-1} \mathbf{S}_2^n\boldsymbol{\ell}_2. \tag{5}$$

The significance of the compatibility conditions in Eqns. (1, 2) is that this position is path independent. Planar crease patterns, such as four-parallelogram origami, are a limiting case with infinite radius of curvature $1/R = 0$, for which

the lattice compatibility conditions in Eqns. (1, 2) are trivially satisfied and the summation for the vertex positions in Eqn. (5) are integer multiples of the primitive lattice vectors.

First-order Compatibility

Consider a linear isometry that changes both the lattice vectors and the lattice rotations, thereby deforming the quasi-cylindrical geometry. We refer to the change in the lattice vector $\boldsymbol{\ell}_\mu \to \boldsymbol{\ell}_\mu + \boldsymbol{\Delta}_\mu$ as the *lattice displacement* and the change in the lattice rotation $\mathbf{S}_\mu \to (\mathbf{1} + \mathbf{L}_\mu)\mathbf{S}_\mu$ as the *lattice angular velocity*. Since $\mathbf{L}_\mu$ is a generator of the rotation group $SO(3)$, it is equivalent to the vector, $\boldsymbol{\Omega}_\mu$ satisfying $L_{\mu,ik} = \epsilon_{ijk}\Omega_{\mu,j}$, so we use lattice angular velocity to refer to $\mathbf{L}_\mu$ and $\boldsymbol{\Omega}_\mu$ interchangeably. In practice, the lattice displacement and the lattice angular velocity are computed via integration along primitive lattice directions averaged over each nodes in the unit cell. However, we proceed assuming we are given such a set of $\boldsymbol{\Delta}_\mu$ and $\boldsymbol{\Omega}_\mu$.

Since linear isometries are compatible along arbitrary paths, they are compatible along paths between cells in particular. Therefore, the expansion of the lattice orientation and position compatibility conditions in Eqns. (1, 2) are satisfied to first order:

$$\mathbf{L}_1\mathbf{S}_1\mathbf{S}_2 + \mathbf{S}_1\mathbf{L}_2\mathbf{S}_2 = \mathbf{L}_2\mathbf{S}_2\mathbf{S}_1 + \mathbf{S}_2\mathbf{L}_1\mathbf{S}_1, \tag{6}$$

$$\boldsymbol{\Delta}_1 + \mathbf{L}_1\mathbf{S}_1\boldsymbol{\ell}_2 + \mathbf{S}_1\boldsymbol{\Delta}_2 = \boldsymbol{\Delta}_2 + \mathbf{L}_2\mathbf{S}_2\boldsymbol{\ell}_1 + \mathbf{S}_2\boldsymbol{\Delta}_1. \tag{7}$$

From linear orientation compatibility, we equate the in-plane components of the lattice angular velocities by rearranging the terms to $\mathbf{L}_1 - \mathbf{S}_2\mathbf{L}_1\mathbf{S}_2^{-1} = \mathbf{L}_2 - \mathbf{S}_1\mathbf{L}_2\mathbf{S}_1^{-1}$. In this form, each lattice angular velocity appears once on its own and once under the similarity transformation of the transverse lattice rotation. Therefore, the components of the lattice angular velocity in the plane normal to the ground state lattice rotation axis satisfy an identical relationship to that of the ground state lattice vectors in Eqn. 4:

$$\boldsymbol{\Omega}_2^\perp = (\mathbf{1} - \mathbf{S}_1^\perp)^{-1}(\mathbf{1} - \mathbf{S}_2^\perp)\boldsymbol{\Omega}_1^\perp. \tag{8}$$

The change in the lattice rotations specify a change in the lattice rotation axis that, by definition, must be invariant under the new lattice rotations $(\mathbf{1} + \mathbf{L}_\mu)\mathbf{S}_\mu(\hat{S} + \delta\hat{S}_\mu) = \hat{S} + \delta\hat{S}_\mu$, where $\delta\hat{S}_\mu \perp \hat{S}$. Therefore, the change in the lattice rotation axis satisfies:

$$\delta\hat{S}_\mu^\perp = (\mathbf{1} - \mathbf{S}_\mu^\perp)^{-1}(\mathbf{L}_\mu\hat{S})^\perp. \tag{9}$$

The implication of Eqn. (8) from first-order orientation compatibility is that the change in the lattice rotation axis is the same in both directions and the lattice rotations stay coaxial to first order $\delta\hat{S}_1 = \delta\hat{S}_2 \equiv \delta\hat{S}$. As for first-order position compatibility, we again have that the projection onto the rotation axis provides no constraints after orientation compatibility is accounted for. However, the in-plane components yield a nontrivial relationship between the lattice stretches and the lattice angular velocity,

$$\boldsymbol{\Delta}_2^\perp = (\mathbf{1} - \mathbf{S}_1^\perp)^{-1}\Big((\mathbf{1} - \mathbf{S}_2^\perp)\boldsymbol{\Delta}_1 + (\mathbf{L}_1\mathbf{S}_1\boldsymbol{\ell}_2)^\perp - (\mathbf{L}_2\mathbf{S}_2\boldsymbol{\ell}_1)^\perp\Big), \tag{10}$$

which depends explicitly on the axial components of both the lattice vectors and lattice angular velocities, distinguishing first-order position compatibility from zeroth-order position compatibility. Expanding the radius of curvature in Eqn. (3) yields two contributions:

$$\delta R_\mu = \frac{\delta|\boldsymbol{\ell}_\mu^\perp|}{2\sin(\eta_\mu/2)} - \frac{R_\mu}{2}\cot(\eta_\mu/2)\delta\eta_\mu, \tag{11}$$

where the change in the lattice rotation angle is the axial component of the lattice angular velocity $\delta\eta_\mu = \boldsymbol{\Omega}_\mu^\parallel \equiv (\boldsymbol{\Omega}_\mu \cdot \hat{S})\hat{S}$, with the superscript $\parallel$ denoting the axial component. We compute the first-order change in the magnitude of the in-plane component of the lattice vector to be the difference between the in-plane component of the lattice stretch and the rotation of the axial component of the initial lattice vector into the plane:

$$\delta|\boldsymbol{\ell}_\mu^\perp| = \frac{1}{|\boldsymbol{\ell}_\mu^\perp|}\boldsymbol{\ell}_\mu^\perp \cdot \big(\boldsymbol{\Delta}_\mu^\perp - \delta\hat{S}|\boldsymbol{\ell}_\mu^\parallel|\big). \tag{12}$$

This illustrates the importance of the axial components appearing in position compatibility. Indeed, direct calculation shows that imposing position compatibility ensures $\delta R_1 = \delta R_2 \equiv \delta R$ and we conclude that any compatible uniform mode retains the cylindrical structure of the ground state while changing the rotation axis and the radius of curvature. This result is compatible with the analysis of Refs. [1, 2], which is distinct from the analysis for parallelograms. In the latter case, first-order orientation compatibility is trivially satisfied which allows for isometries that generate different radii of curvature along the two lattice directions and therefore represent non-cylindrical deformations. However, such modes are incompatible to second-order and therefore require spatial heterogeneity.

CONTINUUM DEFORMATIONS

We consider a continuous cylindrical surface with the ground state embedding:

$$\mathbf{X}(\varphi, z) = R\cos\varphi\hat{x} + R\sin\varphi\hat{y} + z\hat{z}, \tag{13}$$

where R is the radius of curvature and (φ, z) are the surface coordinates. We use the subscripts μ and ν to denote the surface coordinates and compute the tangent vectors ($\mathbf{t}_\mu = \partial_\mu \mathbf{X}$), the normal vector $\hat{n} = \mathbf{t}_\varphi \times \mathbf{t}_z / |\mathbf{t}_\varphi \times \mathbf{t}_z|$, the first fundamental form with components ($I_{\mu\nu} = \mathbf{t}_\mu \cdot \mathbf{t}_\nu$), the second fundamental form with components ($II_{\mu\nu} = \hat{n} \cdot \partial_\mu \mathbf{t}_\nu$), and the shape operator $\mathcal{S} = \mathbf{II}\mathbf{I}^{-1}$:

$$\mathbf{t}_\varphi = -R\sin\varphi\hat{x} + R\cos\varphi\hat{y}, \tag{14}$$
$$\mathbf{t}_z = \hat{z}, \tag{15}$$
$$\hat{n} = -\hat{y}, \tag{16}$$
$$\mathbf{I} = \begin{pmatrix} R^2 & 0 \\ 0 & 1 \end{pmatrix}, \tag{17}$$
$$\mathbf{II} = \begin{pmatrix} -R & 0 \\ 0 & 0 \end{pmatrix}, \tag{18}$$
$$\boldsymbol{\mathcal{S}} = \begin{pmatrix} -\frac{1}{R} & 0 \\ 0 & 0 \end{pmatrix}. \tag{19}$$

The eigenvalues and eigenvectors of the shape operator ($\boldsymbol{\mathcal{S}}\hat{v} = \kappa\hat{v}$) specify the principal curvatures and principal directions, respectively. For the shape operator in Eqn. (19, these are:

$$\kappa_1 = -\frac{1}{R}, \quad \hat{v}_1 = \begin{pmatrix} 1 & 0 \end{pmatrix}, \tag{20}$$
$$\kappa_2 = 0, \quad \hat{v}_2 = \begin{pmatrix} 0 & 1 \end{pmatrix}. \tag{21}$$

Thus, the trace and determinant of the shape operator respectively determine the mean curvature and Gaussian curvature:

$$H = \frac{1}{2}\mathrm{tr}(\boldsymbol{\mathcal{S}}) = -\frac{1}{2R}, \tag{22}$$
$$K = \det(\boldsymbol{\mathcal{S}}) = 0. \tag{23}$$

Given the ground state in Eqn. 13, we consider the infinitesimal change (denoted with the prefix δ) to the vector field:

$$\delta\mathbf{X}(\varphi, z) = A(\varphi, z)(\cos\varphi\hat{x} + \sin\varphi\hat{y}) + B(\varphi, z)(-\sin\varphi\hat{x} + \cos\varphi\hat{y}) + C(\varphi, z)\hat{z}, \tag{24}$$

where A, B, and C determine the deformation in the radial, azimuthal, and axial directions, respectively. It follows from the definitions above that the tangent vectors, first fundamental form, second fundamental form, and shape operator change to first order in δ by the respective amounts:

$$\begin{aligned}\delta\mathbf{t}_\varphi = &\big((\partial_\varphi A - B)\cos\varphi - (A + \partial_\varphi B)\sin\varphi\big)\hat{x} \\ &\big((A + \partial_\varphi B)\cos\varphi + (\partial_\varphi A - B)\sin\varphi\big)\hat{x} + \partial_\varphi C\hat{z},\end{aligned} \tag{25}$$
$$\begin{aligned}\delta\mathbf{t}_z = &(\partial_z A\cos\varphi - \partial_z B\sin\varphi)\hat{x} \\ &+ (\partial_z A\sin\varphi + \partial_z B\cos\varphi)\hat{x} + \partial_z C\hat{z},\end{aligned} \tag{26}$$
$$\delta\mathbf{I} = \begin{pmatrix} 2R(A + \partial_\varphi B) & R\partial_z B + \partial_\varphi C) \\ R\partial_z B + \partial_\varphi C) & 2\partial_z C \end{pmatrix}, \tag{27}$$
$$\delta\mathbf{II} = \begin{pmatrix} \partial_\varphi^2 A - A - 2\partial_\varphi B & \partial_\varphi\partial_z A - \partial_z B \\ \partial_\varphi\partial_z A - \partial_z B & \partial_z^2 A \end{pmatrix}, \tag{28}$$
$$\delta\boldsymbol{\mathcal{S}} = \frac{1}{R^2}\begin{pmatrix} A + \partial_\varphi^2 A & R(\partial_\varphi C + R\partial_\varphi\partial_z A) \\ \partial_\varphi\partial_z A - \partial_z B & R^2\partial_z^2 A \end{pmatrix} \tag{29}$$

.
Importantly, the diagonal components of Eqn. (27), which correspond to the strains $\varepsilon_{\varphi\varphi}$ and ε_{zz} do not appear in Eqn. (29). We use Eqn. (29) to determine the infinitesimal change in the principal curvatures and principal directions:

$$\delta\kappa_1 = \frac{1}{R^2}(A + \partial_\varphi^2 A), \quad \delta\hat{v}_1 = \frac{1}{R}\begin{pmatrix} 0 & \partial_z B - \partial_\varphi \partial_z A \end{pmatrix} \tag{30}$$

$$\delta\kappa_2 = \partial_z^2 A, \quad \delta\hat{v}_2 = \begin{pmatrix} \partial_\varphi C + R\partial_\varphi\partial_z A & 0 \end{pmatrix}. \tag{31}$$

The corresponding changes to the mean and Gaussian curvature are:

$$\delta H = \frac{1}{2R^2}(A + \partial_\varphi^2 A + R^2\partial_z^2 A), \tag{32}$$

$$\delta K = -\frac{1}{R^2}\partial_z^2 A. \tag{33}$$

Since we are interested in the continuum approximation of the homogeneous isometries in quasi-cylindrical origami, the solution must stay cylindrical [1, 2], i.e. the solutions have zero Gaussian curvature. Hence, we require $\partial_z^2 A = 0$ so that Eqn. (33) vanishes. Consequently, the radial scalar field must take the form $A(\varphi, z) = A_0(\varphi) + zA_1(\varphi)$. This simultaneously ensures that the change in the second principal curvature in Eqn. (31) is always zero to first order in the deformation.

We first look for solutions to the breathing mode that we define to change the first principal curvature, but not the two principal directions. This imposes the three conditions:

$$A + \partial_\varphi^2 A = \delta R, \tag{34}$$

$$\partial_z B - \partial_\varphi \partial_z A = 0, \tag{35}$$

$$\partial_\varphi C + R\partial_\varphi\partial_z A = 0. \tag{36}$$

We generally find sinusoidal solutions to the condition in Eqn. (34) for A_0 and A_1, but since we restrict ourselves to homogeneous deformations we determine $A_0 = \delta R$ and $A_1 = 0$. Since $A_1 = 0$, the second condition in Eqn. (35) requires $\partial_z B = 0$ and the third condition in Eqn. (36) requires $\partial_\varphi C = 0$. This implies we have $B = B(\varphi)$ and $C = C(z)$. We determine these scalar fields based on the in-plane strain of the surface to conclude $B(\varphi) = \varphi\big(\varepsilon_{\varphi\varphi}/(2R) - \delta R\big)$ and $C(z) = z\varepsilon_{zz}/2$. The corresponding deformation field is written:

$$\delta\mathbf{X} = \big(\delta R\cos\varphi - \frac{1}{2R}\varphi(\varepsilon_{\varphi\varphi} - 2R\delta R)\sin\varphi\big) + \big(\delta R\sin\varphi + \frac{1}{2R}\varphi(\varepsilon_{\varphi\varphi} - 2R\delta R)\cos\varphi\big)\hat{y} + \frac{1}{2}z\varepsilon_{zz}. \tag{37}$$

We next look for solutions to the shearing mode that we define to change the principal directions but not the principal curvatures. This imposes the three conditions:

$$A + \partial_\varphi^2 A = 0, \tag{38}$$

$$\partial_z B - \partial_\varphi \partial_z A = R\sigma_1, \tag{39}$$

$$\partial_\varphi C + R\partial_\varphi\partial_z A = R\sigma_2. \tag{40}$$

Again, we generally find sinusoidal solutions to the condition in Eqn. (38 for A_0 and A_1, but restrict ourselves to homogeneous deformations and this time we determine $A_0 = A_1 = 0$. Therefore, the second condition in Eqn. (39) requires $\partial_z B = R\sigma_1$ and the third condition in Eqn. (40) requires $\partial_\varphi C = R\sigma_2$, where we take σ_1 and σ_2 to be constant. This implies we have $B = zR\sigma_1 + B(\varphi)$ and $C = \varphi\sigma_2 + C(\varphi)$. We again determine the remaining scalar based on the in-plane strain of the surface to conclude $B(\varphi) = \varphi\varepsilon_{\varphi\varphi}/(2R)$ and $C(z) = z\varepsilon_{zz}/2$. The corresponding deformation field is written:

$$\delta\mathbf{X} = -\frac{1}{2R}(2R^2\sigma_1 z + \varphi\varepsilon_{\varphi\varphi})\sin\varphi\hat{x} + \frac{1}{2R}(2R^2\sigma_1 z + \varphi\varepsilon_{\varphi\varphi})\cos\varphi\hat{y} + \frac{1}{2}(2\sigma_2\varphi + z\varepsilon_{zz})\hat{z}. \tag{41}$$

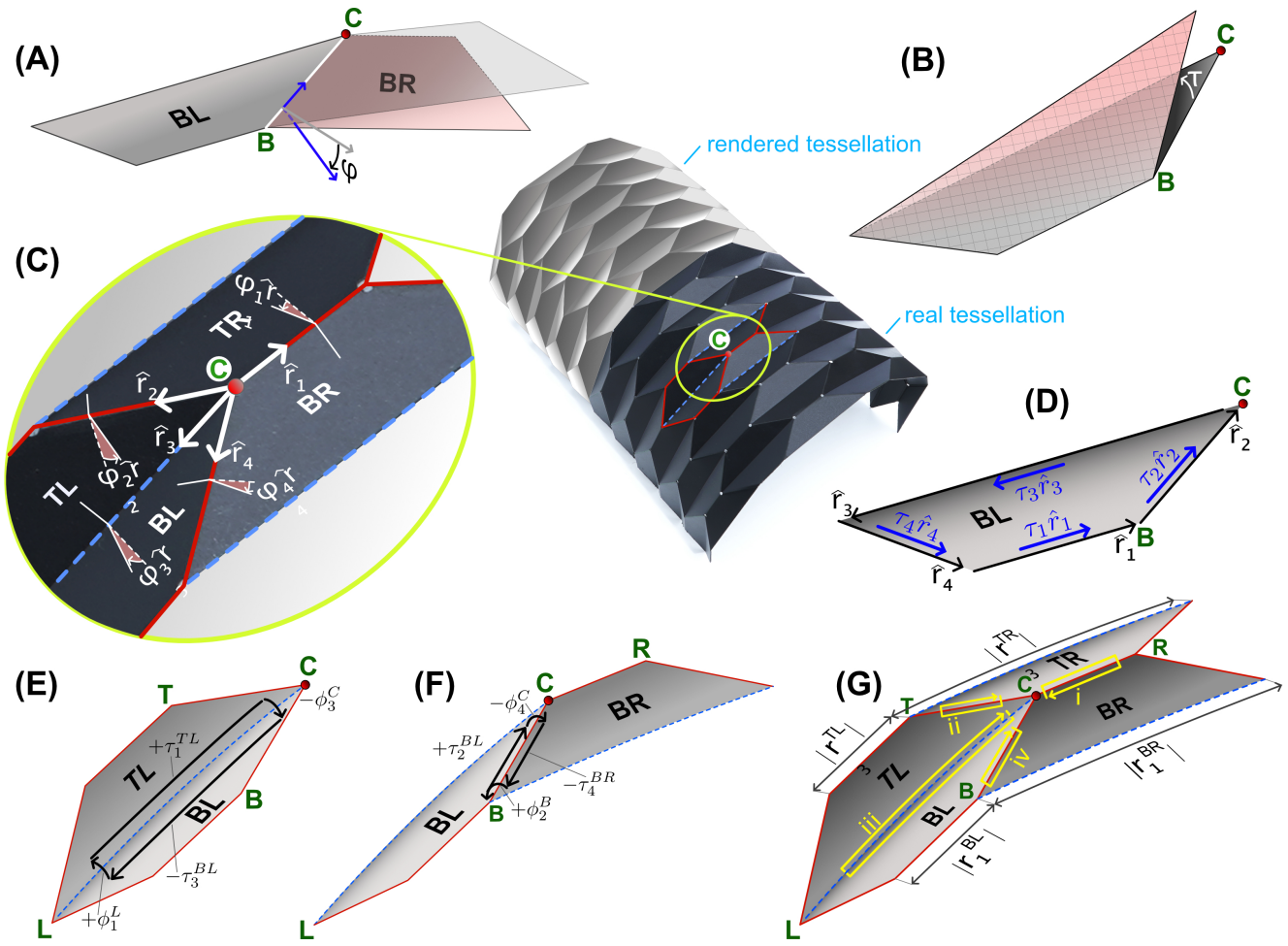

FIG. 2. Illustration of the linear isometry compatibility conditions in the vicinity of a central vertex [C], connecting to the right vertex [R], top vertex [T], left vertex [L], and bottom vertex [B]. These vertices share the top right face [TR], top left face [TL], bottom left face [BL], and bottom right face [BR]. (A) The fold angle ϕ along the edge connecting vertices B and C separated by faces BL and BR. (B) The torsion angle τ along the edge connecting vertices B and C. (C) The four edges emanating from vertex C with unit vectors denoted $\hat{r}_i$ and corresponding fold angles denoted ϕ_i for $i = 1, 2, 3, 4$. (D) The four edges enclosing face BL with unit vectors denoted $\hat{r}_i$ and corresponding torsion angles denoted τ_i for $i = 1, 2, 3, 4$. Loops around edges that (E) have parallel pairs and (F) do not have parallel pairs. (G) The four edge loops used to construct the vertex isometry condition.

LINEAR ISOMETRY COMPATIBILITY CONDITIONS

This Appendix derives the compatibility conditions for linear isometries in TBO. First, the angular velocity field is introduced as a representation of the isometries and its conditions for compatible deformations are presented. Then the compatibility conditions imposed by the separate paths around a single vertex, a single face, and a single edge are considered. Finally, the matrix that maps vertex amplitude degrees of freedom to vertex compatibility constraints, for which the nullspace spans the linear isometries, is derived.

Angular velocity

Since linear isometries do not stretch the panels of the origami, they are spanned by local rotations of the elements of the sheet. In the present work, we characterize these rotations via a vector called the *angular velocity* field $\boldsymbol{\omega}$, i.e., the generator of rotations of line segments on the sheet $d\mathbf{X} \to \boldsymbol{\omega} \times d\mathbf{X}$. However, the components of the angular velocity field cannot be chosen arbitrarily. First, the net change in orientation around any closed path must vanish. While this is trivially satisfied for any continuous and differentiable function, we explicitly impose this orientation compatibility condition to constrain the parameterization of the angular velocity over the piecewise discontinuous

crease pattern. Second, the net displacement around any closed path must also vanish, which ensures the individual panels do not stretch. Together, the orientation and position compatibility conditions constrain the parameterization of the angular velocity field so that the rotations are path independent:

$$\oint d\boldsymbol{\omega} = \mathbf{0}, \tag{42}$$

$$\oint \boldsymbol{\omega} \times d\mathbf{s} = \mathbf{0}. \tag{43}$$

Here, the line integrals are taken over an arbitrary path on the surface of the sheet, which generically crosses various crease lines where the surface tangent vectors can exhibit discontinuities. In this way, the geometry of the crease pattern constrain the linear isometries, and therefore the macroscopic response of the tessellation. It is important to note that non-trivial isometries arise from spatially-varying angular velocity fields whereas constant angular velocity fields generate rigid body rotations.

The angular velocity field is constrained by considering position compatibility in Eqn. (43) on a single polygonal face. Let x_1 and x_2 denote the in-plane coordinates and let x_3 denote the coordinate normal to the plane of the face, then we have from Stoke's theorem (where we use the Einstein summation convention):

$$\begin{aligned}\mathbf{0} = \oint \boldsymbol{\omega} \times d\mathbf{X} &= \oint \hat{e}_i \epsilon_{ijk} \omega_j dX_k \\ &= \iint \hat{e}_i \epsilon_{lmk} \partial_m (\epsilon_{ijk} \omega_j) dA_l \\ &= \iint \hat{e}_i (\partial_j \omega_j dA_i - \partial_i \omega_j dA_j),\end{aligned} \tag{44}$$

where ϵ_{ijk} is the antisymmetric Levi-Civita symbol. By definition, $d\mathbf{A}$ is directed along the x_3 component and therefore $dA_1 = dA_2 = 0$ everywhere so that we are left with:

$$\partial_1 \omega_1 + \partial_2 \omega_2 = 0, \tag{45}$$

$$\partial_1 \omega_3 = \partial_2 \omega_3 = 0. \tag{46}$$

Thus, from Eqn. (46), the out-of-plane component of the angular velocity field is constant over the face. This has the crucial implication that the gradient of the angular velocity field lies in the plane of the face, and therefore must be directed along edges at the intersection of any two faces because this is the only direction that is in the plane of both faces simultaneously. Hence, we parameterize gradients in the angular velocity field using scalars defined on the edges of the crease pattern and evaluate the compatibility conditions by decomposing a generic path into paths around vertices (Fig. 2C), faces (Fig. 2D), and edges (Figs. 2E-F). We introduce one scalar ϕ, called the *fold angle*, to specify changes in the angular velocity between adjacent faces that share a vertex (Fig. 2A). Similarly, we introduce a second scalar, τ, called the *torsion angle*, to specify changes in the angular velocity between adjacent vertices that share a face (Fig. 2B). These two sets of scalars are defined discretely on the edges and are not required to be uniform, i.e., the fold (torsion) angle is generically different on opposite vertices (faces) that share an edge. Physically, the fold angle corresponds to changes in the local dihedral angle on the crease (Fig. 2A) and the torsion angle corresponds to changes in the local orientation of the face (Fig. 2B). We show below that for linear isometries where the folding angles are non-uniform along the crease, there must be non-zero torsion angles that bend the face. This separation of the folding and bending degrees of freedom of the system enables us to distinguish rigid folding modes that do not bend the faces from generic linear isometries that do.

Vertex compatibility

First, consider the path around a four-coordinated vertex shown in Fig. 2C, where we adopt the convention of locally indexing the edges emanating from the vertex $i = 1, 2, 3, 4$ in counterclockwise order around the vertex starting from the rightmost edge. Since the path encloses no area, position compatibility in Eqn. (43) is trivially satisfied. The folding angle on crease i specifies the gradient in the angular velocity $\phi_i \hat{r}_i$ (no summation) between adjacent faces of the crease so that the orientation compatibility condition reads:

$$\oint_{\text{vertex}} d\boldsymbol{\omega} = \sum \phi_i \hat{r}_i = \mathbf{0}. \tag{47}$$

This equation imposes three independent constraints on the four fold angle degrees of freedom, so that there is a one-dimensional solution. As shown in Ref. [3], this solution is obtained by projecting the cross product $\hat{r}_j \times \hat{r}_k$ onto Eqn. (47), thereby eliminating the contributions from crease j and crease k from the equation. Repeating this for each pair of creases reveals:

$$\phi_i = (-1)^i \mathcal{V} \zeta_i, \tag{48}$$
$$\zeta_i \equiv (\hat{r}_{i+1} \times \hat{r}_{i+2}) \cdot \hat{r}_{i+3}, \tag{49}$$

where we introduce the *vertex amplitude*, $\mathcal{V}$, to specify the magnitude of folding at the vertex relative to other vertices in the sheet and we denote the triple products as the *folding coefficients*, ζ_i.

Face compatibility

Second, consider the path around a trapezoidal face shown in Fig. 2D, where we adopt the convention of locally indexing the edges around the face $i = 1, 2, 3, 4$ in counterclockwise order around the vertex starting from the bottom edge. Rather than integrating the displacements around the face, we equivalently consider position compatibility by requiring that the relative displacement of opposite corners is the same along opposing paths. Since the face is polygonal so that the edges lie in the same plane and the angular velocity gradients are strictly in plane by Eqn. (46), orientation compatibility imposes two independent in-plane constraints whereas position compatibility imposes one independent out-of-plane constraint. The torsion angle on crease i specifies the gradient in angular velocity $\tau_i \hat{r}_i$ (no summation) between adjacent vertices of the crease so that orientation and position compatibility read:

$$\oint_{\text{face}} d\boldsymbol{\omega} = \sum \tau_i \hat{r}_i = \mathbf{0}, \tag{50}$$
$$\oint_{\text{face}} \boldsymbol{\omega} \times d\mathbf{s} = \tau_1 \hat{r}_1 \times \mathbf{r}_2 - \tau_4 \hat{r}_4 \times \mathbf{r}_3 = \mathbf{0}. \tag{51}$$

Similar to the condition for vertex compatibility, these equations impose three independent constraints on the four torsion angle degrees of freedom, so that there is a one-dimensional solution. These face compatibility conditions lead to the key distinction of the present work from that of Ref. [3] where the same formalism was applied to the subset consisting of parallelogram-based origami. In that case, the four edges come in two pairs of anti-parallel lines so that imposing identical torsions on opposing edges exactly satisfies orientation compatibility. In the present case there is only one pair of anti-parallel lines, which we take as the odd-indexed edges directed along $\pm\hat{x}_1$. However, the x_2-components of the even-indexed edges must be the same length $|r_2^{x_2}| = |r_4^{x_2}|$ for the odd-indexed edges to be anti-parallel, where the x_3-components vanish for each edge in the polygonal face. Therefore, from position compatibility we have $\tau_4 = \frac{|r_4|}{|r_3|}\tau_1$, after noting that $|r_3| = |r_3^{x_1}|$. Furthermore, the $\hat{x_2}$-component of orientation compatibility reveals $\tau_2 = \frac{|r_2|}{|r_4|}\tau_4 = \frac{|r_2|}{|r_3|}\tau_1$, from which we use the $\hat{x}_1$-component to write $\tau_3 = \tau_1(1 - \frac{|r_2^{x_1}|}{|r_3|} - \frac{|r_4^{x_1}|}{|r_3|})$. Finally, we obtain the general solution to the combined Eqns. (50, 51) after noting that $|r_3| = |r_1| + |r_2^{x_1}| + |r_4^{x_1}|$ when $|r_3| > |r_1|$:

$$\tau_i = \begin{cases} (-1)^i \mathcal{F} |r_{i+2}|, & i \text{ odd} \\ (-1)^i \mathcal{F} |r_i|, & i \text{ even} \end{cases} \tag{52}$$

where we introduce the face amplitudes, $\mathcal{F}$, to specify the magnitude of the torsion on the face relative to other faces in the sheet. In this form, we see the simplification to the solution for parallelograms $\tau_i = (-1)^i |r_i|$ when $|r_1| = |r_3|$.

Edge compatibility

The edges couple the vertex amplitudes and the face amplitudes to their neighbors, which generate an angular velocity on the path around the edge. Since this path encloses zero area and is entirely directed along a single line,

position compatibility is trivially satisfied and orientation compatibility imposes one constraint. We consider a central vertex (C) connected to the right (R), top (T), left (L), and bottom (B) vertices by edges which share the top right (TR), top left (TL), bottom left (BL), and bottom right faces (BR). We maintain the local indexing of the edges relative to a particular vertex or face, and consider paths along odd-indexed and even-indexed edges separately due to the distinct solutions of the torsion angles. For the even-indexed edges (see Fig. 2F), orientation compatibility takes the form:

$$\begin{aligned} \phi_2^B + \tau_2^{BL} - \phi_4^C - \tau_4^{BR} = 0, \\ \phi_2^C + \tau_2^{TL} - \phi_4^T - \tau_4^{TR} = 0. \end{aligned} \tag{53}$$

Since the torsion angles on even-indexed edges have the same length coefficient, the difference in the face amplitudes takes the form:

$$\begin{aligned} |r_2^{BL}|\mathcal{F}^{BL} - |r_4^{BL}|\mathcal{F}^{BR} = |r_4^C|(\mathcal{F}^{BL} - \mathcal{F}^{BR}) = \mathcal{V}^B\zeta_2^B - \mathcal{V}^C\zeta_4^C), \\ |r_2^{TL}|\mathcal{F}^{TL} - |r_4^{TR}|\mathcal{F}^{TR} = |r_2^C|(\mathcal{F}^{TL} - \mathcal{F}^{TR}) = \mathcal{V}^C\zeta_2^C - \mathcal{V}^T\zeta_4^T \end{aligned} \tag{54}$$

which is equivalent to the form taken for edge in a parallelogram-based origami crease pattern. For the odd-indexed edges (see Fig. 2E), orientation compatibility takes the form:

$$\begin{aligned} \phi_1^L + \tau_2^{TL} - \phi_3^C - \tau_3^{BL} = 0, \\ \phi_1^C + \tau_2^{TR} - \phi_3^R - \tau_3^{TL} = 0. \end{aligned} \tag{55}$$

Since the torsion angles on odd-indexed edges have different length coefficients, the difference in the face amplitudes cannot be reduced the way it can for even-indexed edges:

$$\begin{aligned} |r_1^{TL}|\mathcal{F}^{TL} - |r_3^{BL}|\mathcal{F}^{BL} = \mathcal{V}^L\zeta_1^L - \mathcal{V}^C\zeta_3^C, \\ |r_1^{TR}|\mathcal{F}^{TR} - |r_3^{BR}|\mathcal{F}^{BR} = \mathcal{V}^C\zeta_1^C - \mathcal{V}^R\zeta_3^R. \end{aligned} \tag{56}$$

In principle, the even-indexed and odd-indexed edge compatibility conditions provide a complete characterization of the amplitudes that generate linear isometries in trapezoid-based origami. For a tessellation with periodic boundary conditions, the Euler characteristic vanishes because the number of edges is equal to the number of faces plus the number of vertices. Therefore, the compatibility conditions define a square compatibility matrix mapping from the space of face and vertex amplitudes to the space of edge constraints. While square matrices do not generically possess a non-trivial nullspace, the analysis of Ref. [2] showed there is generically one folding mode per rigid body mode compatible with the periodic boundary conditions for triangulated origami tessellations. The face amplitudes in the present work introduce degrees of freedom equivalent to the folding angles on virtual creases that triangulate the trapezoids, but without requiring a specification of the way the face bends. However, in the absence of the face amplitudes, the compatibility matrix for the isometries is generically over-constrained and rigid folding modes cannot exist without the presence of some degeneracy that makes the edge compatibility conditions redundant.

Vertex Isometry Condition

We gain more insight into the character of these linear isometries by summing the constraints on the four edges emanating from the central vertex in Eqns. (54, 56). For the case of parallelograms, where the vertical and horizontal edges constrain the amplitudes equivalently, these four compatibility equations can be added to eliminate the face amplitudes altogether, as shown in Ref. [3], thereby yielding a map from vertex amplitudes to vertex constraints. In the present case, the sum does not generically eliminate the face amplitudes because the lengths entering the horizontal are different on the top and bottom faces. However, if we consider crease patterns where the lengths of the parallel edges entering the odd-indexed edge constraints are equal, $|r_1^{TL} = |r_3^{BL}|$ and $|r_1^{TL}| = |r_3^{BL}|$, then the sum eliminates the face amplitudes altogether yielding the linear isometry vertex condition at the central vertex:

$$\mathcal{V}^C\Big(\frac{\zeta_1^C}{|r_1^{BR}|} + \frac{\zeta_2^C}{|r_2^C|} + \frac{\zeta_3^C}{|r_1^{BL}|} + \frac{\zeta_4^C}{|r_4^C|}\Big) - \mathcal{V}^R\frac{\zeta_3^R}{|r_1^{BL}|} - \mathcal{V}^B\frac{\zeta_2^B}{|r_4^C|} - \mathcal{V}^L\frac{\zeta_1^L}{|r_1^{BL}|} - \mathcal{V}^T\frac{\zeta_4^T}{|r_2^C|} = 0 \tag{57}$$

Since Eqn. (57) is for a generic vertex, the linear isometries must satisfy this condition at every vertex simultaneously. Thus, each vertex provides one degree of freedom and one constraint so that the linear isometries span the nullspace of a linear compatibility matrix. Furthermore, elements of this nullspace generically map to nonzero face amplitudes as determined via the edge compatibility conditions in Eqns. (54, 56).

For this subfamily of crease patterns, we generalize the conclusions from the special case of parallelogram-based origami. We find the same linear isometry with uniform face amplitudes and zero vertex amplitudes. While parallelogram-based crease patterns exhibit two additional linear isometries because of their three translational symmetries, trapezoid-based crease patterns are generically screw-periodic with one translational and one rotational symmetry [1, 2]. Thus, the compatibility matrix constructed from the isometry condition in Eqn. (57) should exhibit a one-dimensional nullspace. While we cannot provide further characterization of the form of this isometry without specification of the crease pattern, we can identify a sufficient, but not necessary, condition for rigid folding modes. When the folding coefficients are uniform along all of the creases so that, e.g., $\zeta_1^C = \zeta_3^R$ in Eqn. (57), this second linear isometry is a rigid folding mode with $\mathcal{V} = 1$ on all of the vertices. A more thorough characterization of the conditions for rigid folding are beyond the scope of the present work.

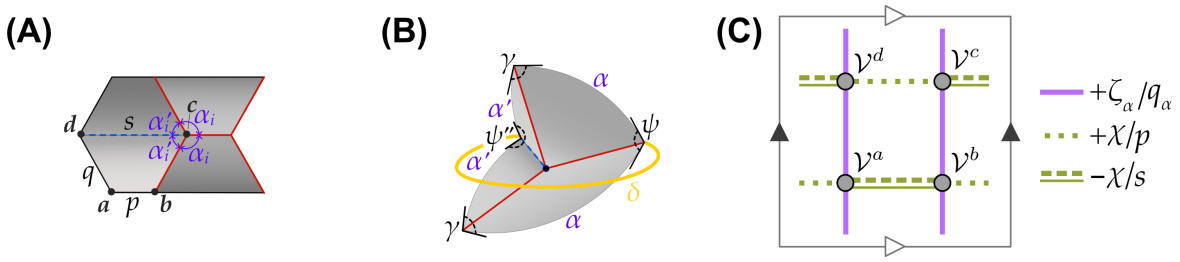

FIG. 3. Miura-derivative TBO. (A) The real-space geometry of the primitive unit cell with edge lengths p, q, and $s = p - 2q\cos\alpha$; and sector angles α and $\alpha' \equiv \pi - \alpha$. (B) The spherical geometry of a vertex in panel A with sector angles α and α'' functioning as sides of a spherical quadrilateral diagonalized by side δ. The interior angles are given by the dihedral angles γ, ψ, and $\psi'' \equiv 2\pi - \psi$. (C) The compatibility diagram for the primitive cell shown in panel A with folding coefficients ζ and χ; the edges couple vertex amplitudes $\mathcal{V}$ distinguished by the superscript.

TBO EXAMPLES

In the following, we determine the relationship between the dihedral angles via spherical trigonometry and use $\arctan(x, y)$ to denote the two-point arc tangent function that determines the angle on the unit circle corresponding to the direction of the vector (x, y) in the xy-plane. We focus on four types of developable origami crease patterns and construct their corresponding compatibility diagrams. Our method extends to non-developable crease patterns directly. We use different colors to indicate couplings with different folding coefficients, which change as the configuration rigidly folds. In contrast, we use dashing and thickness to indicate couplings with the same folding coefficient but are proportional to one another due to a change in sign or a different edge length.

Muira-derivative

The Miura-derivative TBO is a periodic tessellation with four vertices in the primitive cell. Four faces meet at each vertex, two of which subtend a sector angle α and the remaining two of which subtend the supplemental sector angle $\alpha' \equiv \pi - \alpha$. We write the dihedral angle of the crease between corners with sector angles α and α' as γ. The dihedral angles on the remaining two edges are complementary, which we determine via spherical trigonometry as $\psi = 2\arctan\Big(-\cot\alpha(1+\cos\delta)/\sin\delta, \sin\alpha\sin\gamma/\sin\delta\Big)$ and denote the complement as $\psi'' \equiv 2\pi - \theta$ where $\delta = \arccos(\cos^2\alpha + \sin^2\alpha\cos\gamma)$. There are three edge lengths in the primitive cell, which we write p, q, and $s \equiv p - 2q\cos\alpha$. We denote the two folding coefficients as $\zeta \equiv \sin^2\alpha\sin\gamma$ and $\chi \equiv \sin^2\alpha\sin\psi$.

Extended Miura-derivative

The extended Miura-derivative TBO expands upon the Miura-derivative TBO by doubling the size of the primitive cell as shown in Fig. 4A. In addition to the sector angles α and α', this pattern also has sector angles β and $\beta' \equiv 2\pi - \beta$. Consequently, there are three types of vertices as shown in Figs. 4B-D. We denote the dihedral angles as γ_α, γ_β, $\psi_\alpha = 2\arctan\Big(-\cot\alpha(1+\cos\delta)/\sin\delta, \sin\alpha\sin\gamma_\alpha/\sin\delta\Big)$ and $\psi_\beta = 2\arctan\Big(-\cot\beta(1+\cos\delta)/\sin\delta, \sin\beta\sin\gamma_\beta/\sin\delta\Big)$, and $\psi \equiv \arctan\Big(-\cot\alpha(1+\cos\delta)/\sin\delta, \sin\alpha\sin\gamma_\alpha/\sin\delta\Big) + \arctan\Big(-\cot\beta(1+\cos\delta)/\sin\delta, \sin\beta\sin\gamma_\beta/\sin\delta\Big)$, where $\cos\delta = -\cos^2\alpha + \cos^2\alpha\cos\gamma_\alpha = -\cos^2\beta + \cos^2\beta\cos\gamma_\beta$. We denote the folding coefficients $\zeta_\alpha \equiv \sin^2\alpha\sin\gamma_\alpha$, $\zeta_\beta \equiv \sin^2\beta\sin\gamma_\beta$, $\chi_\alpha \equiv \sin^2\alpha\sin\psi_\alpha$, $\chi_\beta \equiv \sin^2\beta\sin\psi_\beta$, and $\chi \equiv \sin\alpha\sin\beta\sin\psi$. We represent the compatibility diagram in Fig. 4E.

Archimedean spiral

The Archimedean spiral generalizes the Miura-derivative TBO by grading the crease pattern so that the sector angles and edge lengths in successive columns vary as indicated by the section of the strip shown in Fig. 5. Each column of the strip has its own sector angle α_i while one edge is always of length p. The remaining edges have lengths q_i satisfying $q_{i+1}\sin\alpha_{i+1} = q_i\sin\alpha_i$, $s_i = p - 2q_i\cos\alpha_i$, and $t_i = p - q_i\cos\alpha_i - q_{i+1}\cos\alpha_{i+1}$. The dihedral

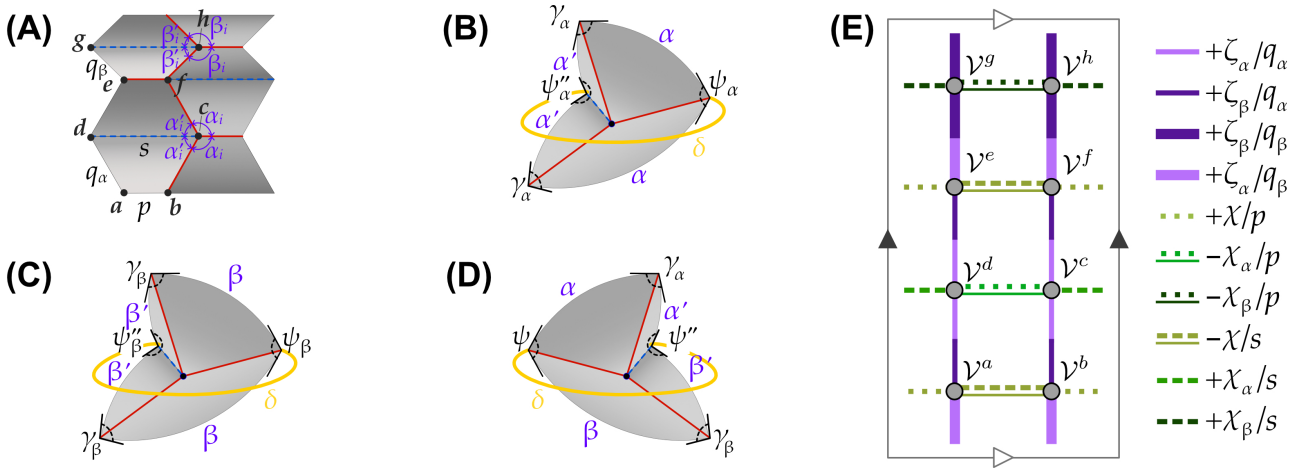

FIG. 4. Extended Miura-derivative TBO. (A) The real-space geometry of the primitive unit cell with edge lengths p, q_α, q_β, and $s = p - 2q_\alpha \cos\alpha = p - 2q_\beta \cos\beta$; and sector angles α, $\alpha' \equiv \pi - \alpha$, β, and $\beta' \equiv \pi - \beta$. (B-D) The spherical geometry of vertices in panel A with the appropriate sector angles functioning as sides of a spherical quadrilateral diagonalized by side δ. The interior angles are given by the dihedral angles γ_α, γ_β, ψ_α, $\psi''_\alpha \equiv 2\pi - \psi_\alpha$, ψ_β, $\psi''_\beta \equiv 2\pi - \psi_\beta$, ψ, and $\psi'' \equiv 2\pi - \psi$. (E) The compatibility diagram for the primitive cell shown in panel A with folding coefficients ζ_α, ζ_β, and χ_α, χ_β, and χ; the edges couple vertex amplitudes $\mathcal{V}$ distinguished by the superscript.

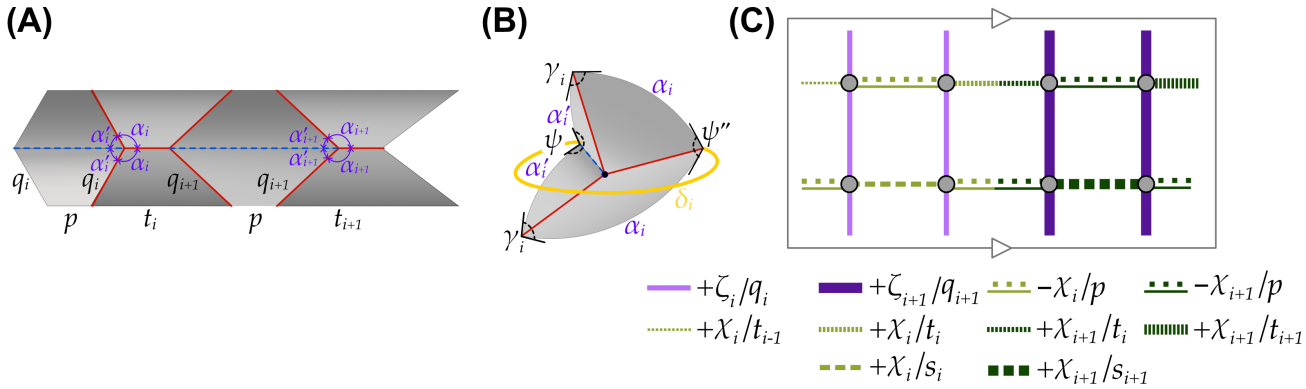

FIG. 5. Archimedean spiral TBO. (A) A section of the primitive cell with sector angles α_i and $\alpha'_i \equiv 2\pi - \alpha_i$ and edge lengths p, q_i, $s_i = p - 2q_i \cos\alpha_i$, and $t_i = p - q_i \cos\alpha_i - q_{i+1} \cos\alpha_{i+1}$ where i labels the column of the strip. (B) The spherical geometry for the vertices in panel A with the appropriate sector angles functioning as sides of a spherical quadrilateral diagonalized by side δ. The interior angles are given by the dihedral angles γ_i and ψ

angles are computed from the spherical polygon shown in Fig. 5B as $\psi_i = 2\arctan\left(\frac{\cot\alpha_i(1+\delta_i)}{\sin\delta_i}, \frac{\sin\alpha_i \sin\gamma_i}{\sin\delta_i}\right)$ where $\cos\delta_i = -\cos^2\alpha_i + \sin^2\alpha_i \cos\gamma_i$ and $\psi_{i+1} = \psi_i$ due to the connectivity of the vertices. We write the two sets of folding coefficients $\zeta_i \equiv \sin^2\alpha_i \sin\gamma_i$ and $\chi_i \equiv \sin^2\alpha_i \sin\psi$. We illustrate the compatibility diagram for a strip of this pattern in Fig. 5C. An extension of the strip would continue the pattern with the horizontal edges increasing in thickness to the right and decreasing in thickness to the left, and the the vertical edges changing in color.

Lemniscate of Bernoulli

The Lemniscate of Bernoulli generalizes the Archimedean spiral by introducing a parallelogram-interface that changes the curvature of the pattern as shown in Fig. 6A. As in the Archimedean spiral, every column of the strip has an edge with length p and the sector angles are denoted α_i where i labels the column. The remaining edge lengths are q_i satisfying $q_{i+1} = \frac{\sin\alpha_i}{\sin\alpha_{i+1}} q_i$, $s_i \equiv p - 2q_i \cos\alpha_i$, and $t_i \equiv p - q_i \cos\alpha_i - q_{i+1} \cos\alpha_{i+1}$. The length of the edges at the parallelogram interface are $\bar{p}$. The dihedral angles are computed from the spherical polygon shown in Fig. 6B as $\psi_i = 2\arctan\left(\frac{\cot\alpha_i(1+\delta_i)}{\sin\delta_i}, \frac{\sin\alpha_i \sin\gamma_i}{\sin\delta_i}\right)$ where $\cos\delta_i = -\cos^2\alpha_i + \sin^2\alpha_i \cos\gamma_i$ and $\psi_{i+1} = \psi_i$ due to the connectivity

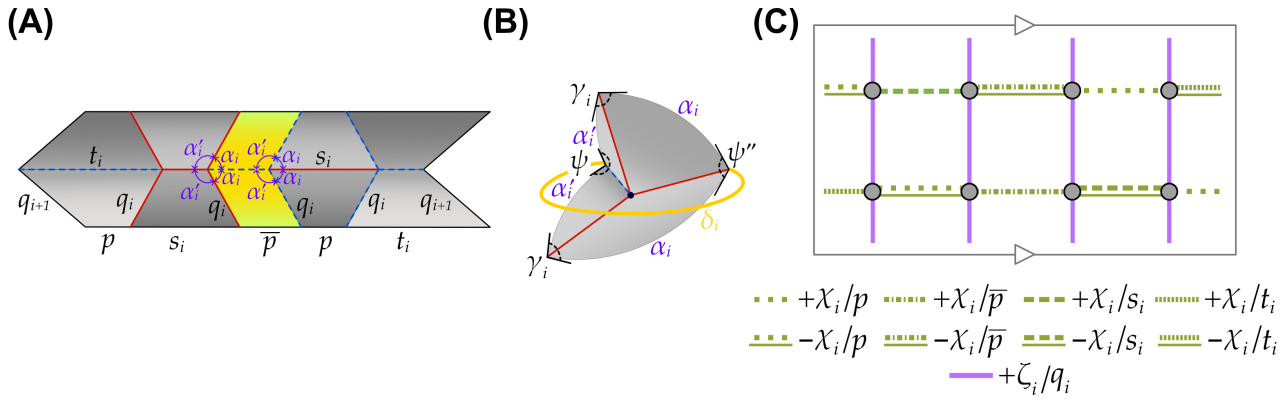

FIG. 6. Lemniscate of Bernoulli TBO. (A) The section of the crease pattern exhibiting a parallelogram interface where the sector angles are labeled α_i and $\alpha_i' \equiv \pi - \alpha_i$ and the edge lengths are labeled p, $\bar{p}$, q_i, $s_i = p - 2q_i \cos\alpha_i$, and $t_i \equiv p - q_i \cos\alpha_i - q_{i+1}\cos\alpha_{i+1}$ where the column index i increases both to the right and to the left of the interface. (B) The spherical geometry of a vertex in panel A with sector angles α_i and α_i divided by the angle δ_i with dihedral angles γ_i and ψ. (C) The compatibility diagram for the section of the crease pattern shown in panel A with folding coefficients $\zeta_i \equiv \sin^2\alpha_i \sin\gamma_i$, $\chi_i \equiv \sin^2\alpha_i \sin\psi$.

of the vertices. We write two sets of folding coefficients $\zeta_i \equiv \sin^2\alpha_i \sin\gamma_i$ and $\chi_i \equiv \sin^2\alpha \sin\psi$. We change from light coloring on the left of the interface to dark coloring on the right of the interface to indicate a change in sign of the coupling coefficients.

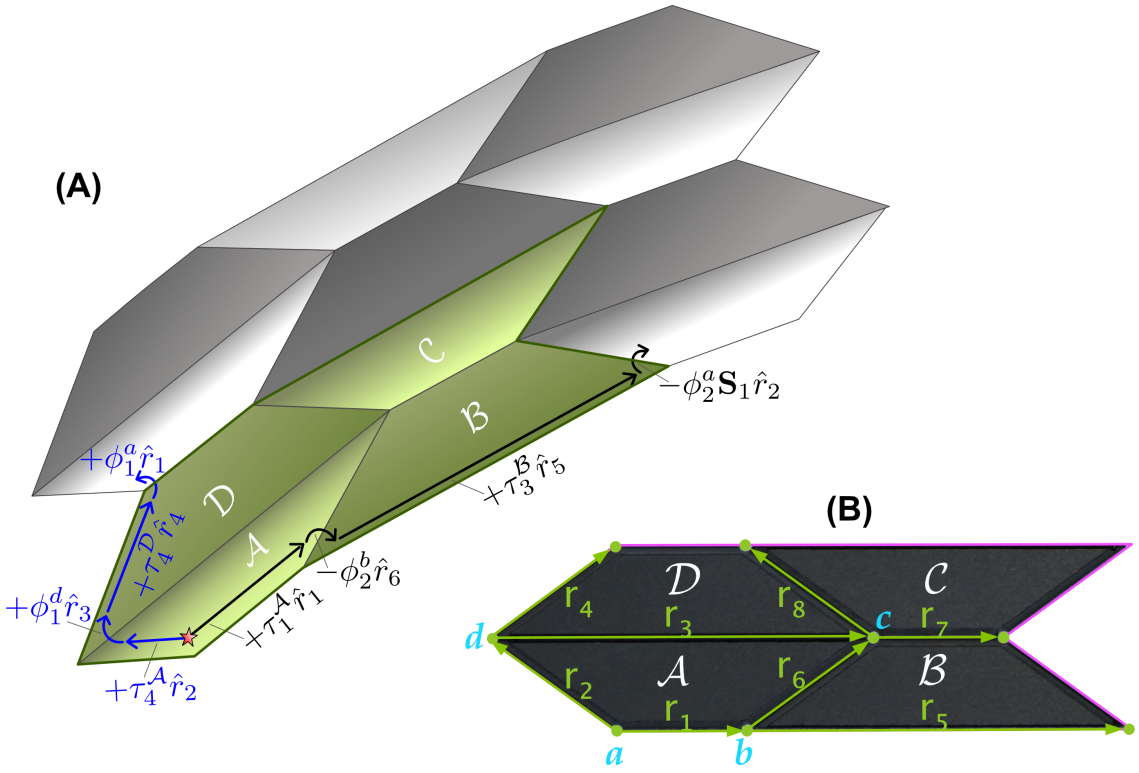

FIG. 7. (A) Illustration of the paths between adjacent cells along the first (black arrows) and second (blue arrows) lattice directions. The change in the lattice angular velocity along these paths are given by the sum of the appropriate torsion angles and fold angles multiplied by their respective edge directions. (B) Notation for calculation of the changes in the lattice vectors and the lattice angular velocities.

MORPH-DERIVATIVE ISOMETRIES

This appendix explicitly computes the coarse-grained fundamental forms for the Morph-derivative TBO. First, we compute the fundamental forms for the ground state. Second, we compute the fundamental forms for the linear isometry that generates the rigid configuration manifold using our amplitude framework. We compare the result to the expansion of the ground state in small changes to the dihedral angle γ. Third, we compute the fundamental forms for the nonrigid isometry.

Ground States

In what follows, we use the eight edges labeled in Fig. 7B

$$\mathbf{r}_1 = (p, 0, 0),$$
$$\mathbf{r}_2 = (q\cos\alpha, q\sin\alpha\cos\frac{\theta}{2}, \sin\alpha\sin\frac{\theta}{2}),$$
$$\mathbf{r}_3 = (s_\alpha, 0, 0),$$
$$\mathbf{r}_4 = (-q\cos\alpha, -q\sin\alpha\cos\frac{\theta}{2}, \sin\alpha\sin\frac{\theta}{2}),$$
$$\mathbf{r}_5 = (-s_\beta\cos\delta, s_\beta\sin\delta, 0),$$
$$\mathbf{r}_6 = (-q\cos\alpha, q\sin\alpha\cos\frac{\theta}{2}, \sin\alpha\sin\frac{\theta}{2}),$$
$$\mathbf{r}_7 = (-p\cos\delta, p\sin\delta, 0),$$
$$\mathbf{r}_8 = (q\cos\alpha, -q\sin\alpha\cos\frac{\theta}{2}, \sin\alpha\sin\frac{\theta}{2}),$$

and the lattice rotation angle

$$\eta = 2(\pi - \delta) \tag{58}$$

to characterize the ground state and deformations along the rigid folding mechanism, where $\mathbf{S}$ is a rotation about the $\hat{z}$-axis by η. From Methods, Morph-derivative TBO of the main text:

$$\begin{aligned}\theta &= 2\arctan\Big(\frac{\cos\beta-\cos\alpha\cos\delta}{\sin\alpha\sin\delta},\frac{\sin\beta\sin\gamma}{\sin\delta}\Big),\\ \psi &= 2\arctan\Big(\frac{\cos\alpha-\cos\beta\cos\delta}{\sin\beta\sin\delta},\frac{\sin\alpha\sin\gamma}{\sin\delta}\Big),\\ \delta &\equiv \arccos(\cos\alpha\cos\beta+\sin\alpha\sin\beta\cos\gamma).\end{aligned} \tag{59}$$

According to our averaging procedure, we compute:

$$\begin{aligned}\bar{\boldsymbol{\ell}}_1 &\equiv \frac{1}{4}\Big((\mathbf{r}_1+\mathbf{r}_5)+(\mathbf{r}_5+\mathbf{S}\mathbf{r}_1)+(\mathbf{r}_3+\mathbf{r}_7)+(\mathbf{r}_7+\mathbf{S}\mathbf{r}_3)\\ &= 2R\sin\frac{\eta}{2}(\cos\varphi\hat{x}+\sin\varphi\hat{y}),\end{aligned} \tag{60}$$

$$\begin{aligned}\bar{\boldsymbol{\ell}}_2 &\equiv \frac{1}{4}\Big((\mathbf{r}_2+\mathbf{r}_4)+(\mathbf{r}_4+\mathbf{r}_2)+(\mathbf{r}_6+\mathbf{r}_8)+(\mathbf{r}_8+\mathbf{r}_6)\\ &= h\hat{z},\end{aligned} \tag{61}$$

where the radius R and height h take the form:

$$R \equiv \frac{\sqrt{\bar{\boldsymbol{\ell}}_1\cdot\bar{\boldsymbol{\ell}}_1}}{2\sin\frac{\eta}{2}} = \frac{1}{4}\Big(p+s_\beta+(p+s_\alpha)\cos\frac{\eta}{2}\Big)\csc\frac{\eta}{2} \tag{62}$$

$$h \equiv |\bar{\boldsymbol{\ell}}_2| = 2q\sin\alpha\sin\frac{\theta}{2}. \tag{63}$$

We then average over the forwards and backwards directions to obtain the tangent vectors in the cell coordinates:

$$\boldsymbol{t}_1 \equiv \frac{1}{2}\big(\mathbf{1}+\mathbf{S}_1^{-1}\big)\bar{\boldsymbol{\ell}}_1 = R\sin\eta\hat{x}, \tag{64}$$

$$\boldsymbol{t}_2 \equiv \bar{\boldsymbol{\ell}}_2 = h\hat{z}. \tag{65}$$

We infer from these equations that the Jacobian has components $J_{\varphi 1}=\csc\eta$ and $J_{z2}=h^{-1}$ and

$$\boldsymbol{t}_\varphi \equiv J_{\varphi 1}\boldsymbol{t}_1 = R\hat{x}, \tag{66}$$

$$\boldsymbol{t}_z \equiv J_{z2}\boldsymbol{t}_2 = \hat{z}, \tag{67}$$

$$\hat{n} \equiv \frac{\mathbf{t}_\varphi\times\mathbf{t}_z}{|\mathbf{t}_\varphi\times\mathbf{t}_z|} = -\hat{y}. \tag{68}$$

The fundamental forms and the shape operator then yield the expected quantities:

$$\mathbf{I} = \begin{pmatrix} R^2 & 0\\ 0 & 1\end{pmatrix}, \tag{69}$$

$$\mathbf{II} = \begin{pmatrix} -R & 0\\ 0 & 0\end{pmatrix}, \tag{70}$$

$$\boldsymbol{\mathcal{S}} = \begin{pmatrix} -R^{-1} & 0\\ 0 & 0\end{pmatrix}. \tag{71}$$

This concludes the characterization of the ground state.

Rigid Isometry

The rigid isometry is represented by the vertex amplitudes $\mathcal{V}^a=\mathcal{V}^b=\mathcal{V}^c=\mathcal{V}^d=1$ and the face amplitudes $\mathcal{F}^{\mathcal{A}}=\mathcal{F}^{\mathcal{B}}=\mathcal{F}^{\mathcal{C}}=\mathcal{F}^{\mathcal{D}}=0$. The folding coefficients are:

$$\zeta \equiv \Big((-\mathbf{S}^{-1}\hat{r}_5)\times(-\hat{r}_4)\Big)\cdot\hat{r}_1 = \sin\alpha\sin\beta\sin\gamma, \tag{72}$$

$$\xi \equiv \Big(\hat{r}_2\times(-\mathbf{S}^{-1}\hat{r}_5)\Big)\cdot(-\hat{r}_4) = \sin^2\beta\sin\psi, \tag{73}$$

$$\chi \equiv \Big(-\hat{r}_4\times\hat{r}_1\Big)\cdot\hat{r}_2 = \sin^2\alpha\sin\theta. \tag{74}$$

Since all of the vertex amplitudes are unity, we write the changes in the dihedral angles on the edges labeled in Fig. 7(B):

$$\phi_1 = -\xi, \quad \phi_2 = \zeta, \quad \phi_3 = +\xi, \quad \phi_4 = \zeta, \quad \phi_5 = -\chi, \quad \phi_6 = \gamma, \quad \phi_7 = +\chi, \quad \phi_8 = \gamma. \tag{75}$$

Next, we need to compute the lattice displacement and the lattice angular velocity in each frame. We show the frame with origin on vertex a oriented according to face $\mathcal{A}$ in Fig. 7(A). The black path indicates the segments used to compute $\mathbf{\Delta}_1$ and $\mathbf{\Omega}_1$ whereas the blue paths indicates the segments used to compute $\mathbf{\Delta}_2$ and $\mathbf{\Omega}_2$. For the rigid mode, all of the torsions are zero so the equations are explicitly written:

$$\mathbf{\Delta}_1 = -\phi_2^b\hat{r}_6\times\mathbf{r}_5, \tag{76}$$

$$\mathbf{\Delta}_2 = +\phi_1^d\hat{r}_3\times\mathbf{r}_4, \tag{77}$$

$$\mathbf{\Omega}_1 = -\phi_2^b\hat{r}_6 - \phi_2^a\mathbf{S}\hat{r}_2, \tag{78}$$

$$\mathbf{\Omega}_2 = +\phi_1^d\hat{r}_3 + \phi_1^a\hat{r}_1. \tag{79}$$

Calculations for the sixteen other cell and orientation combinations follow mutatis mutandis, and we skip to show specific results. For the four orientations with origin at vertex a, we have:

$$\mathbf{\Omega}_1(a,\mathcal{A}) = 2\zeta\cos\frac{\psi}{2}\sin\beta\Big(\sin\frac{\eta}{2}\hat{x} - \cos\frac{\eta}{2}\hat{y}\Big) - 2\zeta\sin\alpha\sin\frac{\theta}{2}\hat{z}, \tag{80}$$

$$\mathbf{\Omega}_1(a,\mathcal{B}) = -2\zeta\sin\alpha\Big(\cos\frac{\theta}{2}\hat{y} + \sin 2\theta\hat{z}\Big), \tag{81}$$

$$\mathbf{\Omega}_1(a,\mathcal{C}) = -2\zeta\sin\alpha\Big(\cos\frac{\theta}{2}\hat{y} - \sin\frac{\theta}{2}\hat{z}\Big), \tag{82}$$

$$\mathbf{\Omega}_1(a,\mathcal{D}) = 2\zeta\cos\frac{\psi}{2}\sin\beta\Big(\cos\frac{\eta}{2}\hat{y} - \sin\frac{\eta}{2}\hat{x}\Big) - 2\zeta\sin\alpha\sin\frac{\theta}{2}\hat{z}, \tag{83}$$

$$\mathbf{\Omega}_2(a,\mathcal{A}) = \mathbf{0}, \tag{84}$$

$$\mathbf{\Omega}_2(a,\mathcal{B}) = \mathbf{0}, \tag{85}$$

$$\mathbf{\Omega}_2(a,\mathcal{C}) = \mathbf{0}, \tag{86}$$

$$\mathbf{\Omega}_2(a,\mathcal{D}) = \mathbf{0}, \tag{87}$$

$$\mathbf{\Delta}_1(a,\mathcal{A}) = s_\beta\zeta\big(\zeta\hat{x} - \zeta\cot\frac{\eta}{2}\hat{y} + \sin\beta\cos\frac{\psi}{2}\big), \tag{88}$$

$$\mathbf{\Delta}_1(a,\mathcal{B}) = 2\zeta\Big(s_\beta\zeta\hat{x} - \big(s_\beta\zeta\cot\frac{\eta}{2} - \frac{p\zeta}{2}\csc\frac{\eta}{2}\big)\hat{y} + \frac{1}{2}(p + 2s_\beta\cos\frac{\eta}{2})\sin\alpha\cos\frac{\theta}{2}\hat{z}\Big) \tag{89}$$

$$\mathbf{\Delta}_1(a,\mathcal{C}) = 2\zeta\Big(s_\beta\zeta\hat{x} - \big(s_\beta\zeta\cot\frac{\eta}{2} - \frac{p\zeta}{2}\csc\frac{\eta}{2}\big)\hat{y} - \frac{1}{2}(p + 2s_\beta\cos\frac{\eta}{2})\sin\alpha\cos\frac{\theta}{2}\hat{z}\Big) \tag{90}$$

$$\mathbf{\Delta}_1(a,\mathcal{D}) = s_\beta\zeta\big(\zeta\hat{x} - \zeta\cot\frac{\eta}{2}\hat{y} + \sin\beta\cos\frac{\psi}{2}\big), \tag{91}$$

$$\boldsymbol{\Delta}_2(a,\mathcal{A}) = q\xi \sin\alpha \cos\frac{\theta}{2}\hat{z}, \tag{92}$$

$$\boldsymbol{\Delta}_2(a,\mathcal{B}) = q\xi \sin\alpha \cos\frac{\theta}{2}\hat{z}, \tag{93}$$

$$\boldsymbol{\Delta}_2(a,\mathcal{C}) = q\xi \sin\alpha \cos\frac{\theta}{2}\hat{z}, \tag{94}$$

$$\boldsymbol{\Delta}_2(a,\mathcal{D}) = q\xi \sin\alpha \cos\frac{\theta}{2}\hat{z}, \tag{95}$$

Averaging over each of the four faces yields:

$$\boldsymbol{\Omega}_1(a) = -2\zeta^2 \csc\frac{\eta}{2}, \tag{96}$$

$$\boldsymbol{\Omega}_2(a) = \mathbf{0}, \tag{97}$$

$$\boldsymbol{\Delta}_1(a) = \frac{\zeta^2}{2}\Big(3s_\beta\hat{x} - \big(p + 3s_\beta\cos\frac{\eta}{2}\big)\csc\frac{\eta}{2}\hat{y}\Big), \tag{98}$$

$$\boldsymbol{\Delta}_2(a) = q\xi \sin\alpha \cos\frac{\theta}{2}\hat{z}. \tag{99}$$

We find $\bar{\boldsymbol{\Omega}}_1$, $\bar{\boldsymbol{\Omega}}_2$, and $\bar{\boldsymbol{\Delta}}_2$ average to the same value at each vertex, while $\bar{\boldsymbol{\Delta}}_1$ averages to cancel the components orthogonal to $\bar{\boldsymbol{\ell}}_1$:

$$\bar{\boldsymbol{\Omega}}_1 = -2\zeta^2 \csc\frac{\eta}{2}, \tag{100}$$

$$\bar{\boldsymbol{\Omega}}_2 = \mathbf{0}, \tag{101}$$

$$\bar{\boldsymbol{\Delta}}_1 = \frac{\zeta^2}{4}\Big(2(p+s_\beta) + 3(p+s_\alpha)\cos\frac{\eta}{2}\hat{x} - \frac{1}{2}\big(4(p+s_\beta)\cos\frac{\eta}{2} + (p+s_\alpha)(1+3\cos\eta)\big)\csc\frac{\eta}{2}\hat{y}\Big), \tag{102}$$

$$\bar{\boldsymbol{\Delta}}_2 = q\xi \sin\alpha \cos\frac{\theta}{2}\hat{z}. \tag{103}$$

This enables computation of the changes in the fundamental forms via construction of the tangent vectors, from which we deduce:

$$\varepsilon_{\varphi\varphi} \equiv \delta I_{\varphi\varphi} = \frac{\zeta^2}{4}R\Big(2(p+s_\beta) + 3(p+s_\alpha)\cos\frac{\eta}{2}\Big)\csc\eta, \tag{104}$$

$$\varepsilon_{zz} \equiv \delta I_{zz} = \xi\cot\frac{\theta}{2}, \tag{105}$$

$$\delta R \equiv \delta I\!I_{\varphi\varphi} + \frac{1}{R}\delta I_{\varphi\varphi} = \frac{\zeta^2}{16}\Big(4(p+s_\beta)\cos\frac{\eta}{2} + (p+s_\alpha)(3+\cos\eta)\Big)\csc^3\frac{\eta}{2} \tag{106}$$

These results are self-consistent in that $\delta\delta R\mathcal{S}_{\varphi\varphi}R^2 = \delta I\!I_{\varphi\varphi} + \delta I_{\varphi\varphi}/R$. However, this result for δR does not agree with the expansion of R about small changes to γ:

$$\delta R \equiv \frac{\partial R}{\partial\eta}\frac{\partial\eta}{\partial\gamma}\delta\gamma = \frac{\zeta^2}{4}\Big(p + s_\alpha + (p+s_\beta)\cos\frac{\eta}{2}\Big)\csc^3\frac{\eta}{2}. \tag{107}$$

Upon further inspection, we find that computing the ground state and the deformed state from any single radius always yields consistent results for the change in the radius. Furthermore, averaging vertices a and d (or, alternatively vertices b and c) also yields consistent results for the change in the vertices. The discrepancy only arises when averaging, e.g., vertices a and b. We find our coarse-graining procedure requires these vertices to be directly summed over rather than averaged to yield consistent results, but we cannot provide an explanation within out theory. The only change from above is $\bar{\Delta}_1 \to 2\bar{\Delta}_1$ from which we have:

$$\varepsilon_{\varphi\varphi} \equiv \delta I_{\varphi\varphi} = \zeta^2 R\Big(p + s_\beta + 2(p + s_\alpha)\cos\frac{\eta}{2}\Big)\csc\eta, \tag{108}$$

$$\varepsilon_{zz} \equiv \delta I_{zz} = \xi\cot\frac{\theta}{2}, \tag{109}$$

$$\delta R \equiv \delta II_{\varphi\varphi} + \frac{1}{R}\delta I_{\varphi\varphi} = \frac{\zeta^2}{4}\Big(p + s_\alpha + (p + s_\beta)\cos\frac{\eta}{2}\Big)\csc^3\frac{\eta}{2}. \tag{110}$$

Nonrigid Isometry

The rigid isometry is represented by the vertex amplitudes $\mathcal{V}^a = \mathcal{V}^b = \mathcal{V}^c = \mathcal{V}^d = 0$ and the face amplitudes $\mathcal{F}^{\mathcal{A}} = \mathcal{F}^{\mathcal{B}} = \mathcal{F}^{\mathcal{C}} = \mathcal{F}^{\mathcal{D}} = 1$. Since all of the face amplitudes are unity, we write the torsion angles on the edges labeled in Fig. 7(B):

$$\tau_1 = -s_\alpha, \quad \phi_2 = q, \quad \phi_3 = -p, \quad \phi_4 = q, \quad \phi_5 = -p, \quad \phi_6 = q, \quad \phi_7 = -s_\beta, \quad \phi_8 = q. \tag{111}$$

Next, we need to compute the lattice displacement and the lattice angular velocity in each frame along the different paths discussed above for the rigid isometry. For the nonrigid mode, all of the folds are zero so the equations for the paths illustrated in Fig. 7(A) are explicitly written:

$$\boldsymbol{\Delta}_1 = \tau_1\hat{r}_1 \times \mathbf{r}_5, \tag{112}$$

$$\boldsymbol{\Delta}_2 = +\tau_2\hat{r}_2 \times \mathbf{r}_4, \tag{113}$$

$$\boldsymbol{\Omega}_1 = \tau_1\hat{r}_1 + \tau_5\mathbf{S}\hat{r}_2, \tag{114}$$

$$\boldsymbol{\Omega}_2 = +\tau_2\hat{r}_2 + \tau_4\hat{r}_4. \tag{115}$$

For this mode, all four orientations at a single vertex yield the same results so we provide the results for four separate vertices:

$$\boldsymbol{\Omega}_1(a) = -s_\alpha\hat{x} - p\big(\cos\frac{\eta}{2}\hat{x} + \sin\frac{\eta}{2}\hat{y}\big), \tag{116}$$

$$\boldsymbol{\Omega}_2(b) = -p\big(\cos\frac{\eta}{2}\hat{x} + \sin\frac{\eta}{2}\hat{y}\big) - s_\alpha\big(\cos\eta\hat{x} + \sin\eta\hat{y}\big), \tag{117}$$

$$\boldsymbol{\Omega}_2(c) = -s_\beta\big(\cos\frac{\eta}{2}\hat{x} + \sin\frac{\eta}{2}\hat{y}\big) - p\big(\cos\eta\hat{x} + \sin\eta\hat{y}\big), \tag{118}$$

$$\boldsymbol{\Omega}_2(d) = -p\hat{x} - s_\beta\big(\cos\frac{\eta}{2}\hat{x} + \sin\frac{\eta}{2}\hat{y}\big), \tag{119}$$

$$\boldsymbol{\Omega}_2(a) = h\hat{z}, \tag{120}$$

$$\boldsymbol{\Omega}_2(b) = h\hat{z}, \tag{121}$$

$$\boldsymbol{\Omega}_2(c) = h\hat{z}, \tag{122}$$

$$\boldsymbol{\Omega}_2(d) = h\hat{z}, \tag{123}$$

$$\boldsymbol{\Delta}_1(a) = -s_\alpha s_\beta\sin\frac{\eta}{2}\hat{z}, \tag{124}$$

$$\boldsymbol{\Delta}_1(b) = -p^2\sin\frac{\eta}{2}\hat{z}, \tag{125}$$

$$\boldsymbol{\Delta}_1(c) = p^2\big(\cos\eta\sin\frac{\eta}{2} - \cos\frac{\eta}{2}\sin\eta\big), \tag{126}$$

$$\boldsymbol{\Delta}_1(d) = s_\alpha s_\beta\big(\cos\eta\sin\frac{\eta}{2} - \cos\frac{\eta}{2}\sin\eta\big), \tag{127}$$

$$\boldsymbol{\Delta}_2(a) = qh\big(\sin\alpha\cos\frac{\theta}{2}\hat{x} - \cos\alpha\hat{y}, \tag{128}$$

$$\boldsymbol{\Delta}_2(b) = qh\big(\sin\alpha\cos\frac{\theta}{2}\hat{x} + \cos\alpha\hat{y}, \tag{129}$$

$$\boldsymbol{\Delta}_2(c) = -qh\big(\sin\alpha\cos\frac{\theta}{2}\hat{x} + \cos\alpha\hat{y}, \tag{130}$$

$$\boldsymbol{\Delta}_2(d) = -qh\big(\sin\alpha\cos\frac{\theta}{2}\hat{x} - \cos\alpha\hat{y}. \tag{131}$$

We average over the four vertices and find

$$\bar{\boldsymbol{\Omega}}_1 = -2R\sin\frac{\eta}{2}\big(\cos\frac{\eta}{2}\hat{x} + \sin\frac{\eta}{2}\hat{y}\big), \tag{132}$$

$$\bar{\boldsymbol{\Omega}}_2 = h\hat{z}, \tag{133}$$

$$\bar{\boldsymbol{\Delta}}_1 = -\frac{1}{2}(p^2 + s_\alpha s_\beta)\sin\frac{\eta}{2}\hat{z}\bar{\boldsymbol{\Delta}}_2 = \mathbf{0}. \tag{134}$$

This enables computation of the changes in the fundamental forms via construction of the tangent vectors, from which we deduce:

$$\varepsilon_{\varphi\varphi} \equiv \delta I_{\varphi\varphi} = 0, \tag{135}$$

$$\varepsilon_{zz} \equiv \delta I_{zz} = 0, \tag{136}$$

$$\sigma_1 \equiv \mathcal{S}_{z\varphi}R = 1, \tag{137}$$

$$\sigma_2 \equiv -\mathcal{S}_{\varphi z}R = -R^2 - \frac{1}{2}s_\alpha s_\beta \sec\frac{\eta}{2}. \tag{138}$$

These results are self-consistent in that $\delta II_{z\varphi} = -\sigma_1 R$ and $\delta I_{z\varphi} = R^2\sigma_1 + \sigma_2$.

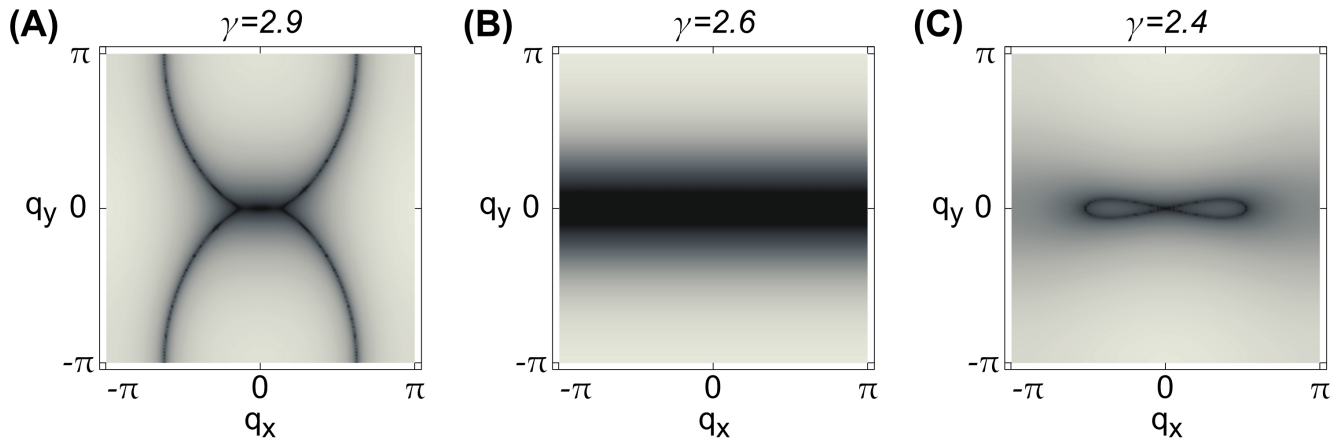

FIG. 8. Bloch-periodic linear isometries for Morph-derivative TBO with (A) $\gamma = 2.9$, (B) $\gamma = 2.6$, and (C) $\gamma = 2.4$.

BLOCH-PERIODIC ISOMETRIES

This appendix shows how to use our amplitude representation for Bloch-periodic modes as previously implemented for the truss representation in Refs. [4, 5]. The idea is to allow the vertex and face amplitudes to vary between cells according to the phase $e^{i\mathbf{q}\cdot\mathbf{n}}$, for wavevector $\mathbf{q} = (q_1, q_2)$ and cell $\mathbf{n} = (n_1, n_2)$. The derivative of Eqn. (57) remains exactly the same, but the construction of the compatibility matrix requires inclusion of these Bloch factors.

Consider, for example, the Morph-derivative TBO geometry. Vertex a connects to vertex b once in the same cell $\mathbf{n} = (0, 0)$ and once in the previous cell $\mathbf{n} = (-1, 0)$, then to vertex d once in the same cell $\mathbf{n} = (0, 0)$ and once in the previous cell $\mathbf{n} = (0, -1)$. Therefore, evaluation of the loop condition on the edges emanating from vertex a includes a factor of e^{-iq_x} on the coupling coefficient χ/p from vertex b in cell $(-1, 0)$ and a factor of e^{-iq_z} on the coupling coefficient ζ/q from vertex d in cell $(0, -1)$. These factors only appear in the columns that map the b vertex and d vertex amplitudes to the a vertex constraint, which takes the form:

$$\mathcal{V}^a\big(2\frac{\zeta}{q} + \frac{\xi}{s_\alpha} + \frac{\chi}{p}\big) - \mathcal{V}^b\big(\frac{\xi}{s_\alpha} + \frac{\chi}{p}e^{-iq_x}\big) - \mathcal{V}^d\frac{\zeta}{q}(1 + e^{-iq_z}) = 0. \tag{139}$$

Note there is no coupling to vertex c since it does not connect to vertex a in the compatibility diagram. Repeating this for the remaining three vertices yields the complete compatibility matrix:

$$\mathbf{C}(q_x, q_z) = \begin{pmatrix} 2\frac{\zeta}{q} + \frac{\xi}{s_\alpha} + \frac{\chi}{p} & -\frac{\xi}{s_\alpha} - \frac{\chi}{p}e^{-iq_x} & 0 & -\frac{\zeta}{q}(1 + e^{-iq_z}) \\ -\frac{\xi}{s_\alpha} - \frac{\chi}{p}e^{iq_x} & 2\frac{\zeta}{q} + \frac{\xi}{s_\alpha} + \frac{\chi}{p} & -\frac{\zeta}{q}(1 + e^{-iq_z}) & 0 \\ 0 & -\frac{\zeta}{q}(1 + e^{iq_z}) & 2\frac{\zeta}{q} - \frac{\xi}{p} - \frac{\chi}{s_\beta} & \frac{\xi}{p} + \frac{\chi}{s_\beta}e^{iq_x} \\ -\frac{\zeta}{q}(1 + e^{iq_z}) & 0 & \frac{\xi}{p} + \frac{\chi}{s_\beta}e^{-iq_x} & 2\frac{\zeta}{q} - \frac{\xi}{p} - \frac{\chi}{s_\beta} \end{pmatrix}. \tag{140}$$

Since Eqn. (140) is a four-by-four matrix, we can represent it algebraically using the Kronecker product ($\otimes$) of the three two-by-two Pauli matrices:

$$\boldsymbol{\sigma}_x = \begin{pmatrix} 0 & 1 \\ 1 & 0 \end{pmatrix}, \quad \boldsymbol{\sigma}_y = \begin{pmatrix} 0 & -i \\ +i & 0 \end{pmatrix}, \quad \boldsymbol{\sigma}_z = \begin{pmatrix} 1 & 0 \\ 0 & -1 \end{pmatrix}, \tag{141}$$

and the identity matrix, denoted $\boldsymbol{\sigma}_0$, as:

$$\begin{aligned}\mathbf{C} = &\frac{1}{2}\Big(4\frac{\zeta}{q} + \frac{\xi}{s_\alpha} - \frac{\chi}{s_\beta} + \frac{\chi-\xi}{p}\Big)\boldsymbol{\sigma}_0 \otimes \boldsymbol{\sigma}_0 + \frac{s_\alpha(p-s_\beta)\chi\cos q_x - s_\beta(p-s_\alpha)\xi}{2ps_\alpha s_\beta}\boldsymbol{\sigma}_0 \otimes \boldsymbol{\sigma}_x \\ &- \frac{(p+s_\beta)\chi\sin q_x}{2ps_\beta}\boldsymbol{\sigma}_0 \otimes \boldsymbol{\sigma}_y - \frac{\zeta(1+\cos q_z)}{q}\boldsymbol{\sigma}_y \otimes \boldsymbol{\sigma}_y - \frac{\zeta\sin q_z}{q}\boldsymbol{\sigma}_y \otimes \boldsymbol{\sigma}_x \\ &+ \frac{1}{2}\Big(\frac{\xi}{s_\alpha} + \frac{\chi}{s_\beta} + \frac{\xi+\chi}{p}\Big)\boldsymbol{\sigma}_z \otimes \boldsymbol{\sigma}_0 - \frac{s_\alpha(p+s_\beta)\chi\cos q_x + s_\beta(p+s_\alpha)\xi}{2ps_\alpha s_\beta}\boldsymbol{\sigma}_z \otimes \boldsymbol{\sigma}_x \\ &+ \frac{(p-s_\beta)\chi\sin q_x}{2ps_\beta}\boldsymbol{\sigma}_z \otimes \boldsymbol{\sigma}_y\end{aligned} . \tag{142}$$

This simplifies for the homogeneous modes $\mathbf{q} = (0,0)$ considered in the main text:

$$\begin{aligned}\mathbf{C}(0,0) = &\frac{1}{2}\Big(4\frac{\zeta}{q} + \frac{\xi}{s_\alpha} - \frac{\chi}{s_\beta} + \frac{\chi-\xi}{p}\Big)\boldsymbol{\sigma}_0 \otimes \boldsymbol{\sigma}_0 + \frac{1}{2}\Big(\frac{\chi}{s_\beta} - \frac{\xi}{s_\alpha} + \frac{\xi-\chi}{p}\Big)\boldsymbol{\sigma}_0 \otimes \boldsymbol{\sigma}_x \\ &- 2\frac{\zeta}{q}\boldsymbol{\sigma}_x \otimes \boldsymbol{\sigma}_x + \Big(\frac{\chi}{s_\beta} + \frac{\xi}{s_\alpha} + \frac{\xi+\chi}{p}\Big)\boldsymbol{\sigma}_z \otimes \boldsymbol{\sigma}_0 - \frac{s_\alpha(p+s_\beta)\chi + s_\beta(p+s_\alpha)\xi}{2ps_\alpha s_\beta}\boldsymbol{\sigma}_z \otimes \boldsymbol{\sigma}_x\end{aligned} . \tag{143}$$

The significance of the Bloch-periodic compatibility matrix in Eqn. (140) is that its nullspace still spans linear isometries. The difference from the homogeneous modes considered in the main text is that the amplitudes corresponding to such a linear isometry are wavevector dependent, so the nullspace must be determined as a function of $\mathbf{q}$. While it is straightforward to do this point-by-point, it is more easy to illustrate the presence of finite wavevector linear isometries by considering the dynamical matrix $\mathbf{D}(\mathbf{q}) \equiv \mathbf{C}(\mathbf{q})^\dagger\mathbf{C}(\mathbf{q})$, where superscript † indicates the conjugate transpose, whose determinant is real-valued and strictly positive (the determinant of $\mathbf{C}$ is also real due to the hidden symmetry discussed in Ref. [2], but changes sign over the Brillouin zone). In Fig. 8, we show density plots of $\det\mathbf{D}$ over the two-dimensional Brillouin zone ($0 \leq q_{x,y} \leq \pi$) scaled logarithmically to highlight lines along which the determinant vanishes, thereby indicating Bloch-periodic linear isometries. We show three distinct configurations of the same crease patterns in panels (A-C) to indicate that the structure of these zero lines is dependent on the configuration. Fig. 8(A) is near the collapsed state, Fig. 8(C) is near the closed state, and Fig. 8(B) is at the transition state $\psi = \pi$ where the mountain/valley assignment switches. We identify this transition state as an important feature of the Morph-derivative TBO where the linear isometries are only allowed to vary in the direction orthogonal to the rotation axis.

[1] T. Tachi, Rigid folding of periodic origami tessellations, Origami **6**, 97 (2015).

[2] J. McInerney, B. G.-g. Chen, L. Theran, C. D. Santangelo, and D. Z. Rocklin, Hidden symmetries generate rigid folding mechanisms in periodic origami, Proceedings of the National Academy of Sciences **117**, 30252 (2020).

[3] J. McInerney, G. H. Paulino, and D. Z. Rocklin, Discrete symmetries control geometric mechanics in parallelogram-based origami, Proceedings of the National Academy of Sciences **119**, e2202777119 (2022).

[4] A. A. Evans, J. L. Silverberg, and C. D. Santangelo, Lattice mechanics of origami tessellations, Physical Review E **92**, 013205 (2015).

[5] P. P. Pratapa, P. Suryanarayana, and G. H. Paulino, Bloch wave framework for structures with nonlocal interactions: Application to the design of origami acoustic metamaterials, Journal of the Mechanics and Physics of Solids **118**, 115 (2018).